Rubio, I., Rodriguez-Millan, M., Marco, M., Olmedo, A., Loya, J.A. (2019) Ballistic performance of aramid composite combat helmet for protection against small projectiles, *Composite Structures,* vol. 226, 111153 doi: https://doi.org/10.1016/j.compstruct.2019.111153

Funding: Ministry of Economy and Competitivenesss of Spain and FEDER program under the Projects: RTC-2015-3887-8 and DPI2017-88166-R.

Ballistic performance of aramid composite combat helmet for protection against small projectiles

I. Rubio [a], M. Rodriguez-Millan[a], M. Marco [a], A. Olmedo[b], J.A. Loya [c]*

[a]*Department of Mechanical Engineering, University Carlos III of Madrid, Avda. de la Universidad 30, 28911, Leganés, Madrid, Spain*

[b]*FECSA Company Calle de Acacias 3, 28703, San Sebastián de los Reyes, Madrid, Spain*

[c]*Department of Continuum Mechanics and Structural Analysis, University Carlos III of Madrid, Avda. de la Universidad 30, 28911, Leganés, Madrid, Spain*

** corresponding author*

Email address: jloya@ing.uc3m.es

Phone number: 916248880

Abstract

This paper focuses on the ballistic performance of aramid composite combat helmet commonly worn by military and security corps, against small projectiles threat. We propose a numerical finite element model for aramid composite protections, considering a multi-layer architecture, able to predict its ballistic behaviour and damage extension. The aim is determining the minimum number of layers required for a correct protection against a given ballistic thread. The constitutive aramid behaviour has been calibrated by means of experimental tests with FSP (Fragment Simulate Projectiles) projectiles and steel spheres on aramid flat plates. Once calibrated, a predictive numerical model of the helmet against different small projectiles and impacted localisations was developed and compared with experimental tests performed in the real head protection.

The results calculated for the absorbed impact energy by the helmet and the induced damage due to small projectiles at different impact location, are in good agreement with experimental results and postmortem helmet analysis, validating the proposed numerical model. The numerical model is thus validated for the design of optimized head protections based on aramid composite.

Keywords

Aramid Composite, Ballistic Impact, Combat helmet, Experimental test, Numerical simulations, Damage extension.

1. Introduction

Aramid composites have become increasingly important in defence and security industries in the last years because of its high stiffness, lightweight and high energy absorption capacity. The use of personal protections has been increased because of the recent rise terrorism, civil and international conflicts since it enables to minimise the morbidity and mortality resulting from

ballistic head injuries. Continuum efforts are being dedicated made to reduce further the helmet weight without diminishing ballistic resistance [1]. The design of helmets to achieve strictest requirements combining impact resistance and reasonable weight is currently one of the primary concerns of military and security industry.

Development of combat helmet is commonly evaluated regarding impact velocity and back face deformation according to the standards NIJ STANDARD 0106.01 for ballistic helmets [2] and STANDARDIZATION AGREEMENT (STANAG) 2920: Ballistic Test Method for personal armour materials and combat clothing [3]. The combat helmets users may be subjected to various hazards such as different ammunitions or impact of shrapnel and shell fragments.

The development of an excellent quality combat helmet involves an expensive and long-time experimental campaign. Furthermore, manufacturers must continually be adapted and updated the combat helmet in line with end-user needs in continuous evolution. The complexity of the experimental tests, involving expensive experimental devices such as a ballistic gas gun, justifies the use of numerical models. Modelling of the high-speed impact of projectiles on combat helmet requires the development of detailed composite models as well as the analysis of their associated response and failure mechanisms to predict the ballistic behaviour.

Therefore, experimental tests combining numerical simulations may become a proper methodology to develop combat helmet. However, few studies focused on developing a complete methodology analysing different parameters such as areal density and bullet's dimensions [4–6]. Tham et al.[4] carried out experiments and simulations on the ballistic impact of a Kevlar helmet using spherical projectiles of 11.9 g at 205 m/s. Moreover, Full-Metal Jacketed (FMJ) 9 mm bullet at 358 m/s and Fragment Simulating Projectile (FSP) were numerically used to analyse the mechanical behaviour of a combat helmet. Tan et al. [5] carried out both experiments and numerical simulations of frontal and lateral ballistic impacts on a headform equipped with Advanced Combat Helmet (ACH) using 11.9 g spherical steel projectile at 220 m/s, analysing the damage induced using computed tomography (CT) technique. Recently, Rodriguez-Millan et al. [6] analysed experimentally and numerically the mechanical behaviour of aramid plates and shell combat helmet according to NIJ STANDARD 0106.01 and STANAG 2920. The good accuracy observed between predictions and experiments proved the ability of the models developed as a design tool. In these researches [4-6], there is no analysis of mechanical behaviour of different thickness or geometry of projectile.

According to the STANAG 2920 standard, the analysis of the V50 velocity can be carried out for different projectile geometries, highlighting the FPS and sphere geometries since cylinders or FSP (57%) and spheres (20%) are the most commonly found shapes in soldiers wounded by IED. Spheres (70%) are found more commonly than cylinders (17%) in soldiers wounded by RPGs or mines [7]. Most studies are focused on the ballistic behaviour of flat specimens [7–9]. Nayak et al. [8,9] carried out experiments and numerical simulations on the ballistic impact of 10mm thick aramid composite by a 7.62 mm armour-piercing projectile at different impact velocities. Analysis of damage was developed and concluded that the value and duration of contact force tend to increase when the impact velocity is close to the ballistic limit and thus enhancing the extent of delaminating and the core damage area as compared to high impact velocities.

Colakoglu et al. [10] determined experimentally and numerically the backside deformation and penetration speed for 4 mm thick Kevlar 29/Polivnyl Butyral using 9 mm FMJ bullet and STANAG 2920 projectile, respectively.

Others researchers focus on analysing combat helmet without experimental tests [11–13]. Van Hoof et al. [11] numerically evaluated the ballistic impact response of composite helmets. They concluded that the predicted backplane deformation was more significant for the helmet than for flat panels fabricated from the same material. The helmet simulations also indicated that the impact event is very localised, and its effects are restricted to the impacted area. The global motion of the helmet is negligible compared to that of the backplane. Lee and Gong [12] developed numerical simulations to evaluate the protection efficiency of combat helmet considering different interior cushioning systems. Li et al. [13] developed a finite element-based computational model for simulating the ballistic performance of the Advanced Combat Helmet (ACH) to analyse different variables: size of helmet, impact angle and impact locations. They concluded that at the same bullet impact velocity, the small-size helmet has the most significant backface deformation and the worst impact location was found for a frontal impact. Palta et al. [14] carried out numerical simulations of the Advanced Combat Helmet under FSP with 1.1g, FMJ with 9 g and .223 rifle impacts. They found that although the ACH protects against 9-mm bullet impacts, it is inadequate under the impact of .223 rifle impact. Also, different authors [15, 16,17,18,19] centered their studies in combat helmet design and behaviour with helmet-head interaction with biomechanical requeriments. In particular, Palomar et al. [16] presented a numerical model consisting of a helmet and a human head validated with experimental data from literature. They considered different head injury criteria and discusses about the influence of the relative size helmet and head and the equivalence between standard damage parameters and brain damage have been highlighted. Aare and Kleiven [17] focus on the effect of helmet shell stiffness and diffetent impact angles on load levels in human head during impact event. Tse et al. [18, 19] conducted a series of ballistic impact simulations of FMJ projetiles on validated human head model which include head kinematics and biomechanical metrics, with combat helmet in order to analyse head injuries involved on ballistic impact threats.

In the present work, the experimental test is performed on aramid plates and combat helmets using two different projectiles: FSP and spheres, recommended by STANAG 2920 to obtain the V50 velocity [3]. The analysis joint effect that target geometry, projectile geometry, impact velocity and localisation have on the penetration mechanisms and induced damage.

As main contribution, a validated numerical finite element model to predict the ballistic and damage response of a more than twenty layers combat helmet subjected to ballistic impact is developed. In literature, helmet shell has been usually modelled with only one or few layers through the thickness to reduce computational cost [5,6,14,16,20-22]. Here, each layer is modelled with one element in the direction orthogonal to the laminate, being the layers connected by cohesive interaction. This particularity allowed to calculate the damage extension and back-face deformation, validated with computed tomography (CT) scan.

For this purpose, the materials and experimental setup are presented in Section 2. The numerical model is developed and calibrated through experimental tests on flat-plates

performed according to STANAG 2920 for different thickness and projectiles in Section 3. For the same type of projectiles, the predicted numerical results for the helmet under ballistic impact are compared with real impact tests showing the accuracy of the model and its suitability to be used as a designing tool in Section 4. An analysis of the thickness influence, projectile and impact zone is analysed in Section 5, and finally, conclusions are stated in the last section.

2. Calibration tests

This section introduces the methodology followed in the development of the material model calibration. Two different projectiles and two areal density material protections were considered.

2.1. Protection material

Flat-plates and combat helmet shell are moulded from aramid plies in a thermosetting Polyvinyl Butyral Phenolic (PVB) matrix. The main features of this material are its high strength, excellent high energy absorbing capacity and good strength-to-weight ratio and it is used in aerospace and military industries, particularly in personal armour composites for protection from ballistic forces.

Flat-plates of 100 × 100 mm^2 and two different areal densities were considered in the calibration part. The first thickness, denoted as thick plate, corresponds to the helmet laminate configuration of 8.86 kg/m^2. The second one, thin plate, corresponds to half-thickness with 4.43 kg/m^2.

2.2. Experimental set-up

Impact tests on plates are conducted using a pneumatic 7.62 mm calibre gas gun to launch .22 FSP projectiles of mass 1.1g and 7,5 mm spherical steel projectiles of mass of 1.7g onto aramid composite, see Figure 1. Perforation tests are performed with impact velocities in the range of 350 m/s < V_0 < 800 m/s. It should be noted that, for all the tests performed, the projectiles showed an absence of plastic straining, damage or erosion after the impact.

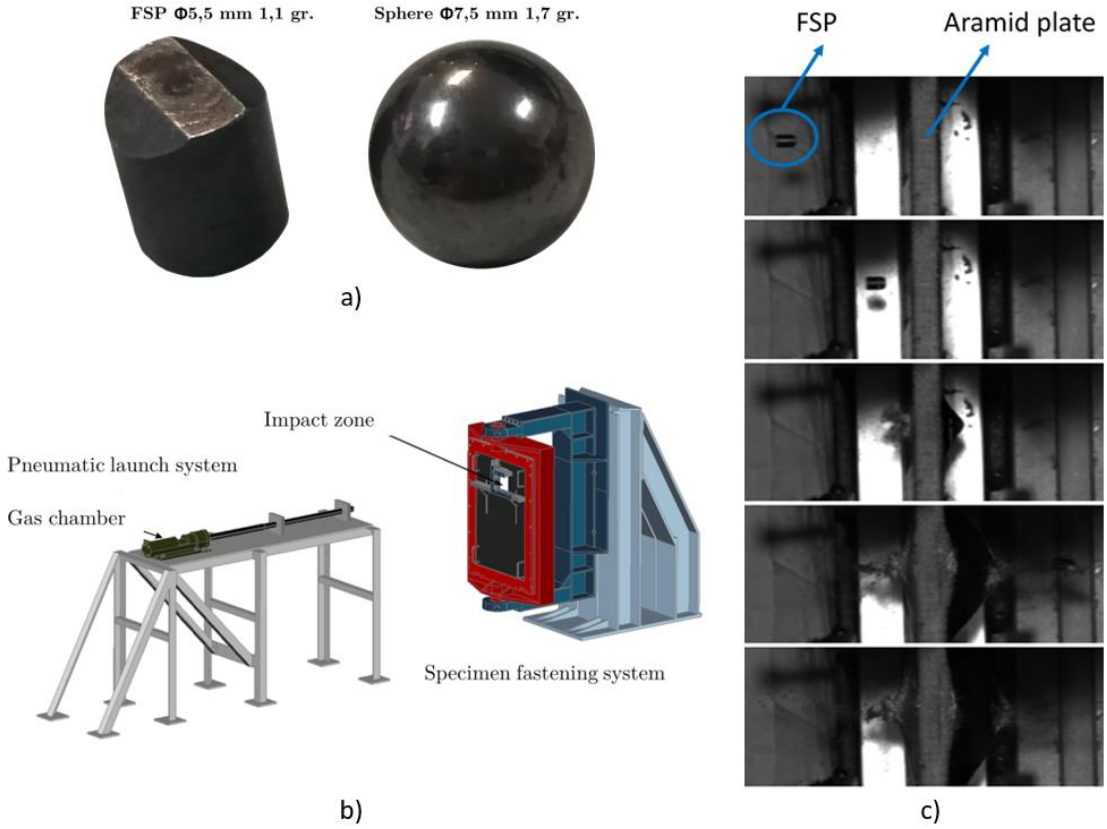

Figure 1. Experimental setup of impact on plate. a) Projectiles; b) Pneumatic launch system and fastening system; c) Impact event recorded

Specimens are clamped in their perimeter with not sliding effects observed during tests. A *Photron FastCam SA-Z* digital high-speed camera placed perpendicular to the specimen, is used to measure the impact projectile velocity, V_i, and the residual one, V_r, when it perforates the target. The selected frame rate (28000 frames per second, fps) and the resolution 1024 x 744 pixels are chosen based on early testing, allowing a proper focus on the images.

The experimental results obtained for aramid plates of different areal density are presented in Table 1. An in-depth analysis of the experimental data is carried out in the following section.

FSP (1.1g)				**Sphere (1.7g)**			
4.43 kg/m²		**8.86 kg/m²**		**4.43 kg/m²**		**8.86 kg/m²**	
V_i (m/s)	**V_r(m/s)**	**V_i (m/s)**	**V_r(m/s)**	**V_i (m/s)**	**V_r(m/s)**	**V_i (m/s)**	**V_r(m/s)**
370	0	640	0	337	0	557.8	0
430	0	696	0	350	0	608.7	0
437	0	697	0	363	0	624.2	167
448	134	700	151	376	0	633.6	240
470	266	717	225	383	116	667.5	332
498	295	719	296	408	208	684.7	385
512	355	720	297	447	289	714.8	469
515	329	728	311	507	399	824.4	563
541	371	730	345	--	--	--	--
657	523	759	414	--	--	--	--

Table 1. Experimental data of impact tests on aramid plates.

3. Numerical model

The mechanical behaviour of the composite aramid model under impact conditions is calibrated for FSP and spherical steel projectiles with the previous experimental data.

The numerical model is developed in the FE code ABAQUS/Explicit using a Lagrangian approach, allowing efficient reproduction of the dynamic loading processes. Three solids are involved in the high-velocity impact test: projectile, fixture structure and the target. The dimensions and geometries of the target and projectiles are the same as used in experiments.

Due to the symmetry of the problem, the numerical model was reduced using ¼ symmetry with the corresponding computational cost reduction.

3.1. Aramid composite constitutive model

The mechanical behaviour of aramid composite is assumed elastic up to failure, whose properties are shown in Table 2.

E_1 (GPa)	E_2 (GPa)	E_3 (GPa)	G_{12} (GPa)	G_{13} (GPa)	G_{23} (GPa)	ν_{12} (-)	ν_{13} (-)	ν_{23} (-)	ρ (kg/m^3)
22.0	22.0	9.0	0.77	5.34	5.34	0.25	0.33	0.33	1230

Table 2. Mechanical properties of aramid composite [23]

Failure is predicted using a modification of Hou et al. [24] failure criteria which is based on Chang-Chang model [25] implemented in a VUMAT user subroutine, equations 1-3. The failure criteria is based on quadratic form, help to account for in-plane and out of plane failure modes, Figure 2.

The failure modes are presented below:

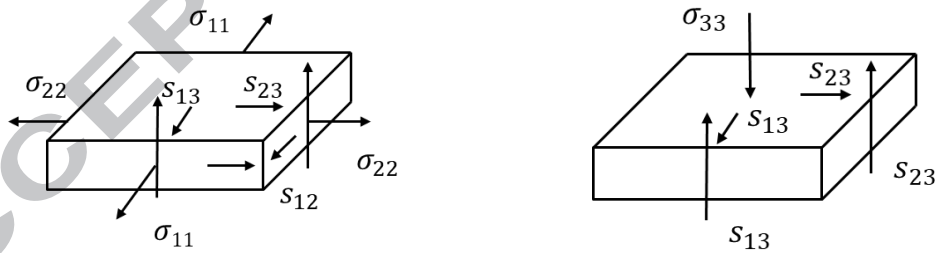

a) b)

Figure 2. Stress components distribution that's participates in each failure modes. a) In plane tension distribution. b) Out of plane tension distribution.

- In-Plane failure modes

  - Fibre failure in direction 1

$$d_{f1} = \left(\frac{\sigma_{11}}{X_{1T}}\right)^2 + \left(\frac{\sigma_{12}}{S_{12}}\right)^2 + \left(\frac{\sigma_{13}}{S_{13}}\right)^2 \quad (1)$$

  - Fibre failure in direction 2

$$d_{f2} = \left(\frac{\sigma_{22}}{X_{2T}}\right)^2 + \left(\frac{\sigma_{12}}{S_{12}}\right)^2 + \left(\frac{\sigma_{23}}{S_{23}}\right)^2 \quad (2)$$

- Out-of-Plane failure modes

  - Failure in direction 3

$$d_3 = \left(\frac{\sigma_{33}}{Z_c}\right)^2 + \left(\frac{\sigma_{13}}{S_{13}}\right)^2 + \left(\frac{\sigma_{23}}{S_{23}}\right)^2 \quad (3)$$

where σ_{11}, σ_{22}, and σ_{33}, are the stresses in a longitudinal, transverse and through-thickness direction respectively; σ_{12}, σ_{23}, and σ_{13} are the shear stresses; X_{1T}, X_{2T} and Z_c are, respectively, the tensile strengths in warp, weft and out of plane directions; S_{12}, S_{13}, and S_{23} are the transverse shear strengths. Failure occurs when any damage variable, d_i , reaches a value equal to 1.

The degradation of elastic properties could lead to distorted elements involving numerical problems. Thus, the model requires the use of an element erosion criterion. The stresses on a damaged element drop to values close to zero while large deformations appear. These elements do not contribute to the strength or the stiffness of the plate, but they can cause lack of convergence during simulation and instability problems. The erosion criterion based on maximum strain criteria was implemented in the VUMAT subroutine to remove the distorted elements. After each time increment, the strains were evaluated, and the element was removed if one of the strains reached a critical value. Thus, numerical problems were avoided, and at the same time, only strongly damaged elements were deleted retaining resistant elements. Other authors have used this method with element deletion at similar works [5,17-19,21,26-28]

The parameters for failure model has been obtained from Gower et al. [23] and presented in table 3.

S_{1t} (MPa)	S_{1c} (MPa)	S_{2t} (MPa)	S_{2c} (MPa)	S_{3t} (MPa)	S_{3c} (MPa)	S_{12} (MPa)	S_{13} (MPa)	S_{23} (MPa)
800	80	800	80	1200	1200	77	898	898

Table 3. Failure properties of aramid composite [23]

3.2. Mesh definition and boundary conditions

3.2.1. Projectiles

The following two kinds of projectiles were considered:

- 1.1 g *Fragment-Simulating Projectile (FSP): It* was made of AISI 4340 steel. Due to no plastic deformation, melting or erosion has been observed on the projectile during impact event, a linear elastic behavior was assumed (E = 210 GPa, ν = 0.3 and ρ = 7850 kg/m^3). This definition reduces the computational cost required. C3D8R elements with average size equal to 0.25 mm was used (Fig. 3a).

- 1.7 g *Spherical steel projectile:* spherical steel projectiles are defined with C3D8R elements and average size equal to 0.25 mm (Fig. 3b). As in the FSP model, it was also considered as linear elastic.

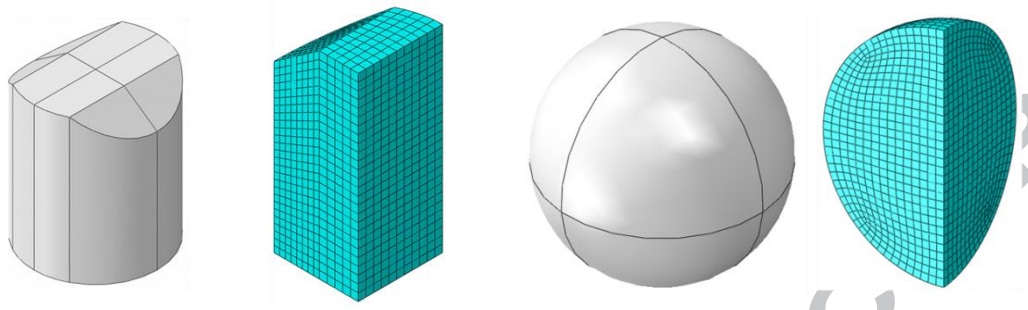

a) b)

Figure 3. Numerical model of a) FSP and b) spherical steel projectile.

3.2.2. Aramid flat-plate model

The mesh plate includes a total number of 8090 elements per layer. Each layer is meshed with hexahedral elements with reduced integration (C3D8R) and with an element per layer through the thickness. The mesh is refined at the zone around the impact area defined by a square of 17 × 17 mm^2 (2-3 times the projectile diameter) with an aspect ratio of elements of 0.81. Out of this region, the element size is increased up to 1.5 mm characteristic length (Fig. 5). A mesh sensitivity analysis was carried out in order to minimize the error in the obtained results and the computational cost.

A interaction between consecutive layers is defined with a cohesive surface. It is based on a quadratic traction-separation law (eq. 4) implemented in ABAQUS/CAE (Fig. 5),

$$\left(\frac{t_n}{t_n^0}\right)^2 + \left(\frac{t_s}{t_s^0}\right)^2 + \left(\frac{t_t}{t_t^0}\right)^2 \geq 1 \tag{4}$$

being the normal (t_n^0) and tangential (t_s^0, t_t^0) threshold stresses for Aramid/PVB composites presented in Table 6

For this model, the damage evolution law for the cohesive surface is based on the fracture energy dissipated during the damage process. The used damage evolution law is:

$$\left(\frac{G_n}{G_n^c}\right)^{\alpha} + \left(\frac{G_s}{G_s^c}\right)^{\alpha} + \left(\frac{G_t}{G_t^c}\right)^{\alpha} = 1 \tag{5}$$

where G_n, G_s and G_t are, respectively, the released rate energies in normal and shear directions, and G_n^c, G_s^c and G_t^c are the corresponding critical values, and, α, is a parameter model that need to be calibrated.

There is not much literature about cohesive properties of Aramid/PVB composites, in particular for the damage evolution law parameters. The fracture energy in the normal direction, G_n^c is obtained from [29] using the relation between the stress intensity factor K_I^c and the Young's modulus E_{ph} of phenolic resin, being ν the Poisson's coefficient in a plane laminated

$$K_I^C = \sqrt{\frac{E_{ph} G_n^c}{1-\nu^2}} \cong \sqrt{E G_n^c} \quad (\nu^2 \approx 0.1) \tag{6}$$

E_{ph} (GPa)	K_I^C (MPa$\sqrt{\text{m}}$)	G_n^c (N/mm)
2.76 – 4.83	0.79 – 1.21	0.22 – 0.30

Table 4. Range of values for E_{ph}, K_I^C and G_n^c obtained from [29]

The fracture energy in shear direction, G_t^c and G_s^c, are calculated from the contact-force history (Fig 4) obtained from the experimental tests developed in [30],

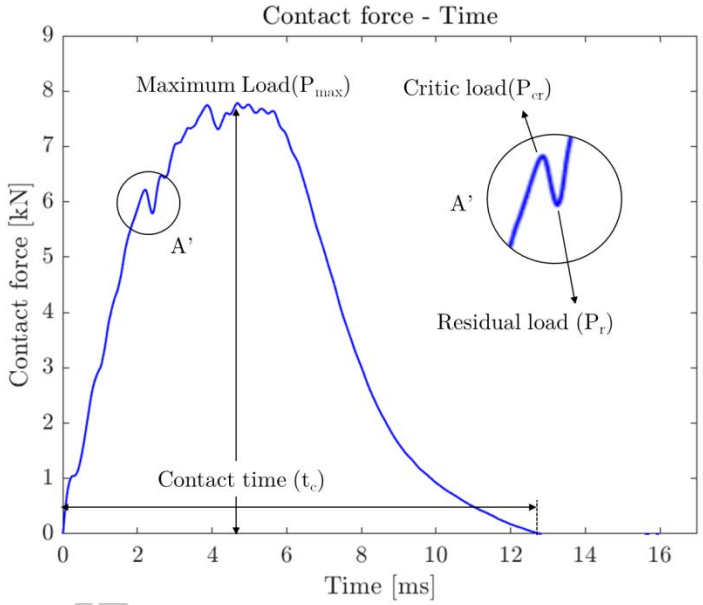

Figure 4. Maximum load, critical load and residual load at low-velocity test.

Here, the critical value of the load, P_{cr}, is the maximum value previous a notable drop of the load in curve, and it is related with the fracture energy in shear direction G_{II}^c (equivalent to G_t^c and G_s^c) using the following analytical expression [31],

$$P_{cr} = \sqrt{\frac{8\pi^2 E z^3}{9(1-\nu^2)} G_{II}^c} \tag{7}$$

where E and ν are the elastic modulus and the Poisson's coefficient in the plane of the laminated, respectively, and z is the thickness of the laminated. Table 5 shows the results obtained for both areal densities studied at different impact energy, E_{imp}:

Thick plate, 8.86 kg/m^2			Thin plate, 4.43 kg/m^2		
E_{imp} [J]	P_{cr} [N]	$G_t^c; G_s^c; G_{II}^c$[N/mm]	E_{imp} [J]	P_{cr} [N]	$G_t^c; G_s^c; G_{II}^c$[N/mm]
46	6410	0.49	19	2277	0.50
77	6217	0.46	37	2143	0.44
92	5878	0.41	55	2297	0.51

119	6252	0.47		
139	5810	0.40		
156	6802	0.50		
173	6645	0.53		
Average G_{II}^c		0.47	Average G_{II}^c	0.48

Table 5. G_{II}^c values derived from experimental test in [30]

The values of G_n^c G_s^c and G_t^c selected to produce the most consistent results based on residual velocity and back face deformation according to the bounds obtained are shown in Table 6.

G_n^c (J/mm^2)	$G_t^c = G_s^c$ (J/mm^2)	t_n^0 (MPa)	$t_t^0 = t_s^0$ (MPa)	α
0.24	0.47	34.5	9.0	1

Table 6. Cohesive properties used in numerical model.

The contact between the projectile and the plate is defined with penalty contact algorithm and hard contact model [32]. The ‘‘hard contact’’ option allows adjusting automatically the stiffness generated by the ‘‘penalty contact algorithm’’, to minimise penetration without adversely affecting the time increment. Concerning frictional effects, it is assumed a dynamic frictional coefficient μ equal to 0.3 between steel and composite.

The fastening system consists on a tip of 7 mm diameter and a profile 50 x 11 mm (symmetry applied) made of steel. Both parts were considered as a rigid body to reduce computational cost.

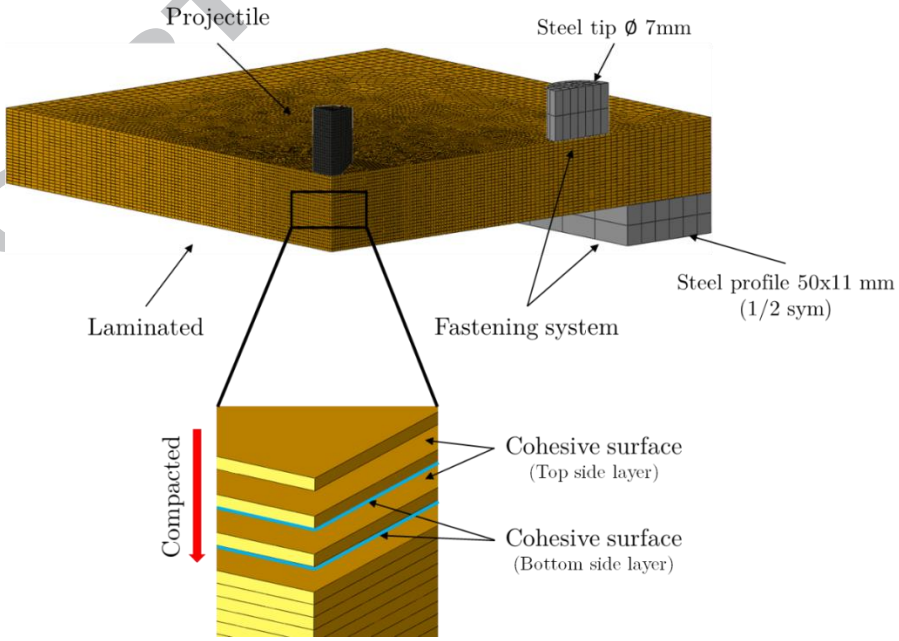

Figure 5. Complete model used in the numerical simulations of FSP impact.

3.3. Numerical calibration

The numerical model presented for aramid composite were calibrated with experimental tests in terms of the ballistic limit, residual velocity and failure modes by qualitative method.

A mesh sensitivity analysis was performed, finding that in the thickness direction, one element per layer allows to simulate the perforation experiments accurately.

3.3.1. Ballistic curves

A comparison between the experimental and numerical ballistic curves (residual velocity, V_r , versus impact velocity, V_i, for both different areal densities and projectiles is presented in Fig. 6. It is can be observed that the numerical model reproduces faithfully the energy loss of projectile, in terms of velocity when it impacts on aramid plates.

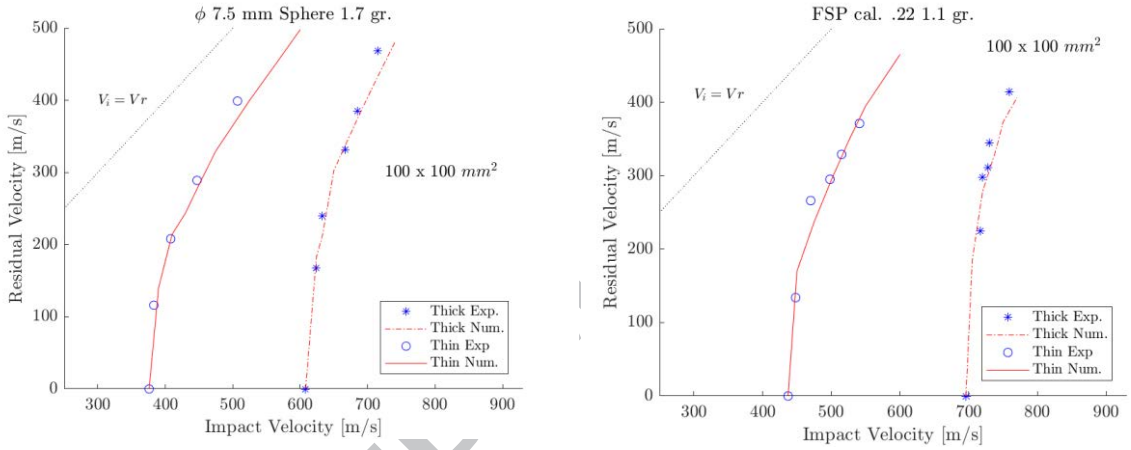

a) b)

Figure 6. Residual velocity versus impact velocity comparison between experiments and numerical simulations for: a) FSP projectile; and b) spherical steel projectile.

For FSP on thin plates, the ballistic limit for experimental tests is 437 m/s and 436 m/s is the numerically predicted. For thick plates, the experimental and numerical ballistic limit match at 696 m/s. In the case of steel sphere projectile, the ballistic limit for thin plates in experimental test and numerical simulations are 376 m/s and 374 m/s, respectively; meanwhile, it increases up to 608 m/s for thick plates in both cases.

Attending to the general agreement for the ballistic curves for both projectiles and areal density materials considered, the numerical model for the aramid composites is considered calibrated in the range of velocity impact analysed.

3.3.2. Failure Modes

To analyse the different material failure mechanisms associated with the projectile during the perforation event, the cross-section of penetrated plates has been considered. Depending on the predominant failure mechanism, the impact event can be divided into different stages. The primary failure mechanism is driven by shear plugging and compression due to the projectile impact on the target surface. As the projectile penetrates, bulge formation on the back face is formed, and delamination is generated between different layers along the thickness. Finally, the

projectile exits through the back face due to the tensile breakage of the last fibres. Figure 6 shows the different perforation mechanisms observed during the tests associated with the projectile velocity.

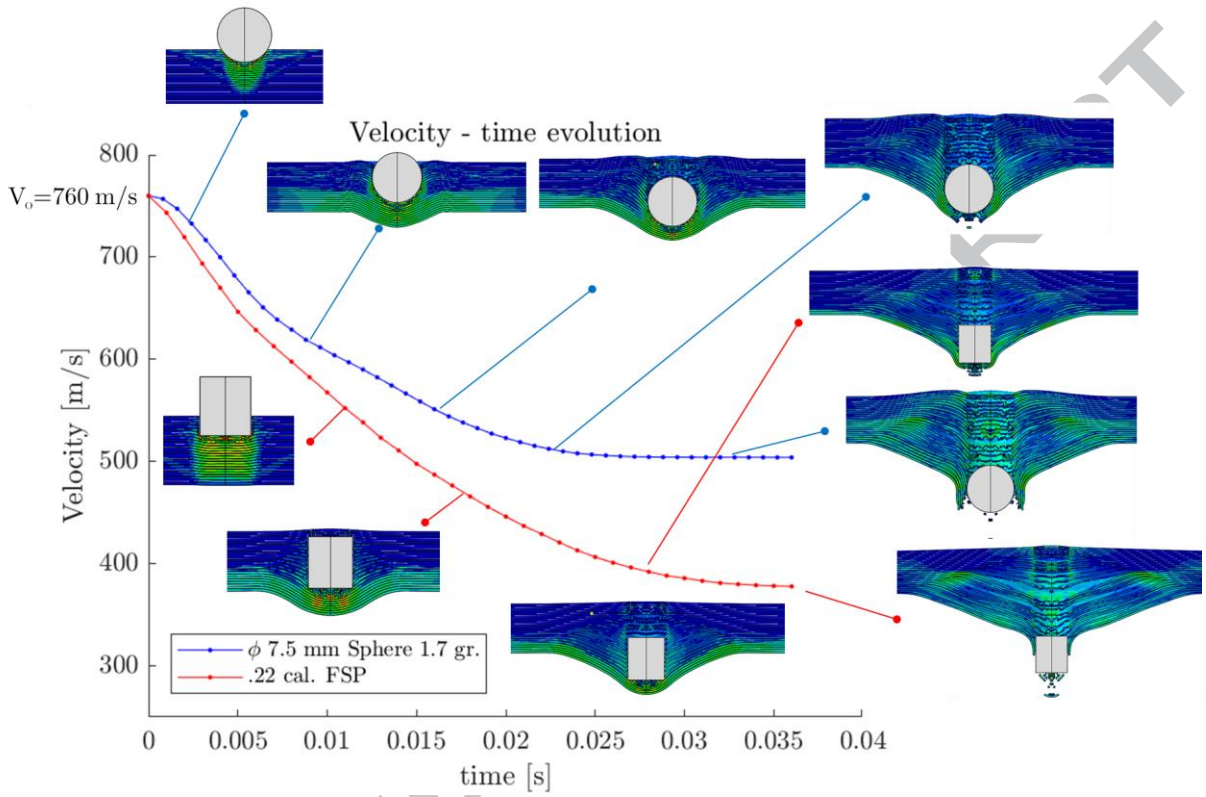

Figure 6. Evolution of the projectile velocity with the time associated and the failure modes at each instant.

Figure 7 illustrates a qualitative comparison of the failure mechanisms during the impact process on the aramid plate for FSP and sphere projectile.

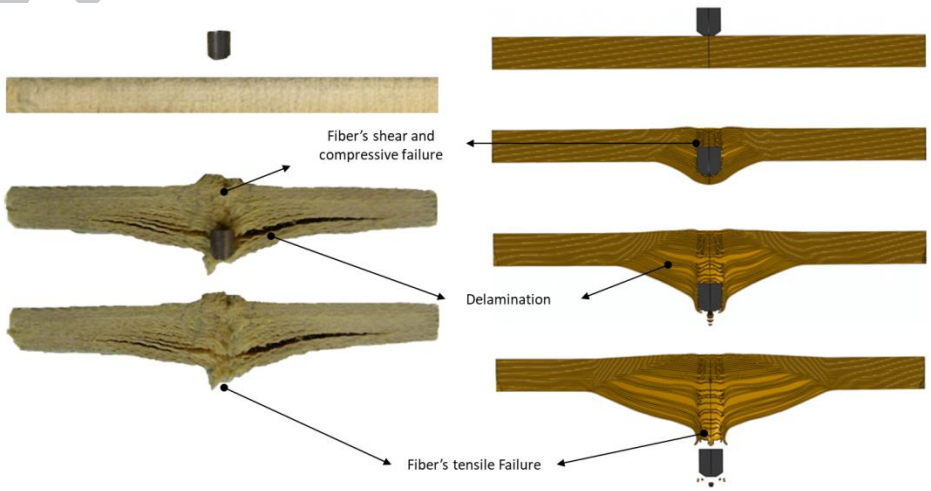

a)

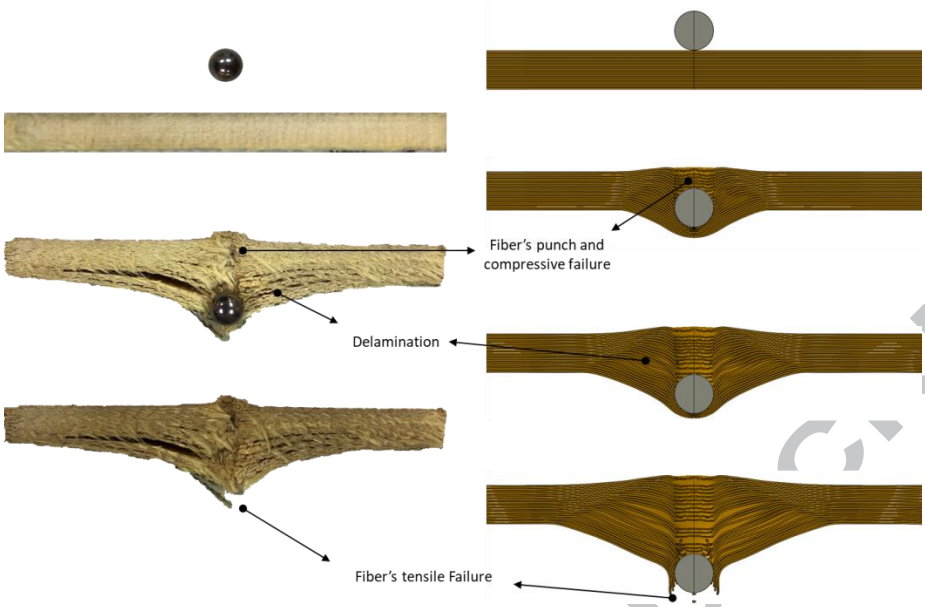

b)

Figure 7. Comparison of failure modes between experiments and numerical simulations.

a) FSP b) Steel sphere.

3.3.3. Back Face Displacement.

The maximum experimental back-face displacement (BFD) during the impact process is obtained using the high-speed camera records, see Figure 8. It can be observed that BFD increases with the velocity up to near the ballistic limit for both projectiles studied. This is because most of the kinetic energy of the projectiles is transferred to the deformation mechanisms (general bending). However, for impact velocities above the ballistic limit, most of the kinetic energy is associated with local failure mechanisms (i.e. compression or shearing plugging) and BFD decreases to a constant value. This behaviour has also been observed in other materials on similar impact tests [33,34].

Numerical simulations show the same trend as experimental tests for complete or non-complete perforation (above and below the ballistic limit). In the case of FSP projectile, the experimental BFD value is 24.3 mm, being 21.0 mm in numerical simulation (13.4% error). For sphere projectiles, experimental BFD was 23.84 mm respect to 22.0 mm for the numerical simulations (7.7% error). Attending to trends prediction and confined dispersion, the developed numerical model can be considered that properly reproduces the behaviour of BFD.

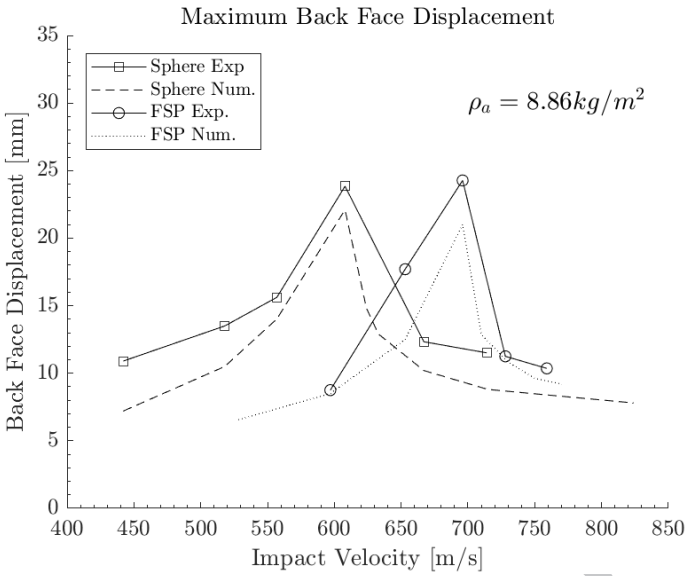

Figure 8. Maximum back face deformation of experimental and numerical results for both projectiles used.

4. Evaluation of the combat helmets ballistic behavior

In this section, experimental ballistic tests are conducted to obtain the ballistic curves and damage extension on combat helmets for the projectiles used previously. These values are compared with the numerical predictions obtained using the previous calibrated parameters.

4.1. Experimental set-up

Two experimental devices are used to carry out the tests according to the projectile. For FSP projectiles, tests are carried out according to STANAG 2920 at the Impact Laboratory of the Universidad Carlos III de Madrid following a similar methodology as presented in section 2 of this work. FSP and sphere projectiles are impelled with a gas-gun against the helmet, supported in the lateral zones (Figure 9). Tests are recorded using a high-speed camera located perpendicular to the impact zone to obtain the impact and residual velocity.

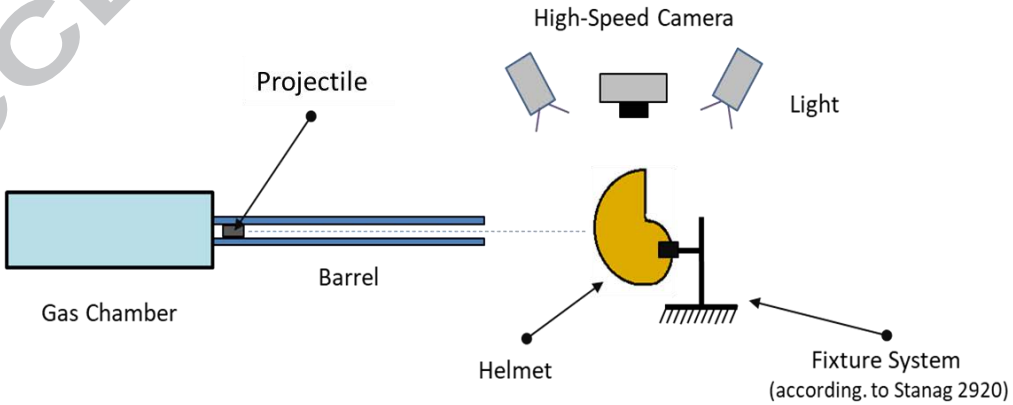

Figure 9 .Scheme of experimental set-up for ballistic impact on combat helmets

4.2. Impact tests

This section is divided according to the used projectile for clarity. The numerical results obtained for the helmet are presented and compared with experimental data. In Section 6 we discuss the results.

4.2.1. Fragment (FSP) 1.1g

First of all, some impact tests are conducted in different zones of the helmet, as is observed in Figure 10a, to determine an experimental V50 of 697m/s. A summary of experimental results is shown in Figure 10b.

a)

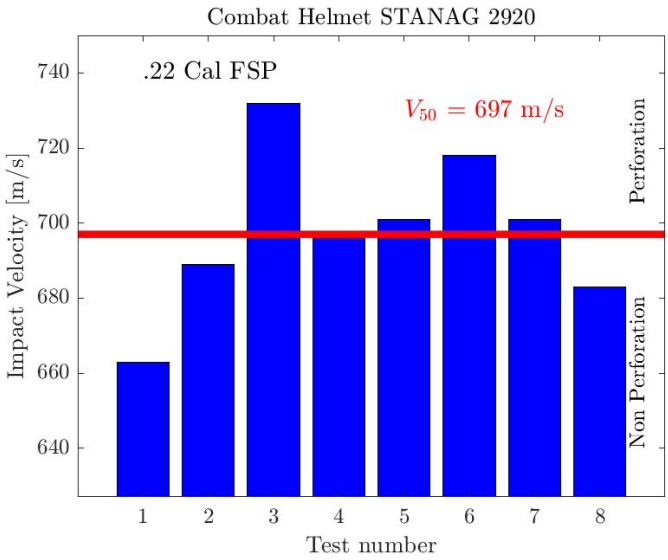

b)

Figure 10. a) Final stage of the combat helmet for STANAG 2920 tests (the impact zone in red) and b) Impact velocities of the STANAG 2920 tests and V50 velocity.

Additionally, eight shots have been carried out on two combat helmets in a range of impact velocities above the ballistic limit, from 760 m/s to 810 m/s, guaranteeing the required complete penetration to obtain the residual velocity. Table 8 shows the experimental results (V_o-V_r) and the localization of the impact. In some few tests, the residual velocity measurements failed due to the impossibility to clearly distinguish the projectile.

Impact velocity V_i (m/s)	Residual velocity V_r (m/s)	Impact Localization
769	414	Frontal
762	469	Rear
782	331	Right lateral
772	not measure	Left lateral

775	not measure	Top
775	not measure	Frontal
802	530	Rear
807	414	Right lateral

Table 8. Experimental tests carried out in combat helmet for FSP projectile.

Numerical results will be analysed at the same time that spherical projectile results in order to compare the impact location and projectile influence.

4.2.2. Spherical steel projectile

Experimental tests with spherical steel projectiles are conducted on two combat helmets. A total of 10 shots (two per impact location) in a range of impact velocities from 616 m/s to 679 m/s are performed above the ballistic limit of the material to obtain residual velocities. Table 9 shows experimental results (V_i-V_r) and the localization of the impact.

Impact velocity V_i (m/s)	**Residual velocity V_r (m/s)**	**Impact Localization**
616	98	Top
631	315	Right lateral
633	327	Frontal
635	321	Rear
640	304	Right lateral
641	242	Frontal
656	307	Top
662	307	Left lateral
671	410	Rear
679	408	Left lateral

Table 9. Experimental data of impact tests on combat helmets using sphere steel projectiles.

4.3. Numerical impact modelling on helmets

Four impact situations were studied: Frontal, Top, Rear and Lateral impact locations. In order to reduce the computational cost, ½ symmetry has been applied in the Frontal, Top and Rear cases, meanwhile the complete helmet is considered for the Lateral impact situation (left and right side are equivalent). As in the calibration flat-plate model, each layer of the helmet is meshed with C3D8R elements with one element per layer through the thickness, keeping constant the same number of elements per layer. The mesh is refined at the zone around the impact area, defined by an around 17 × 17 mm^2 square with elements of 0.81 aspect-ratio. Elements distribution around the impact zone can be observed in Figure 11.

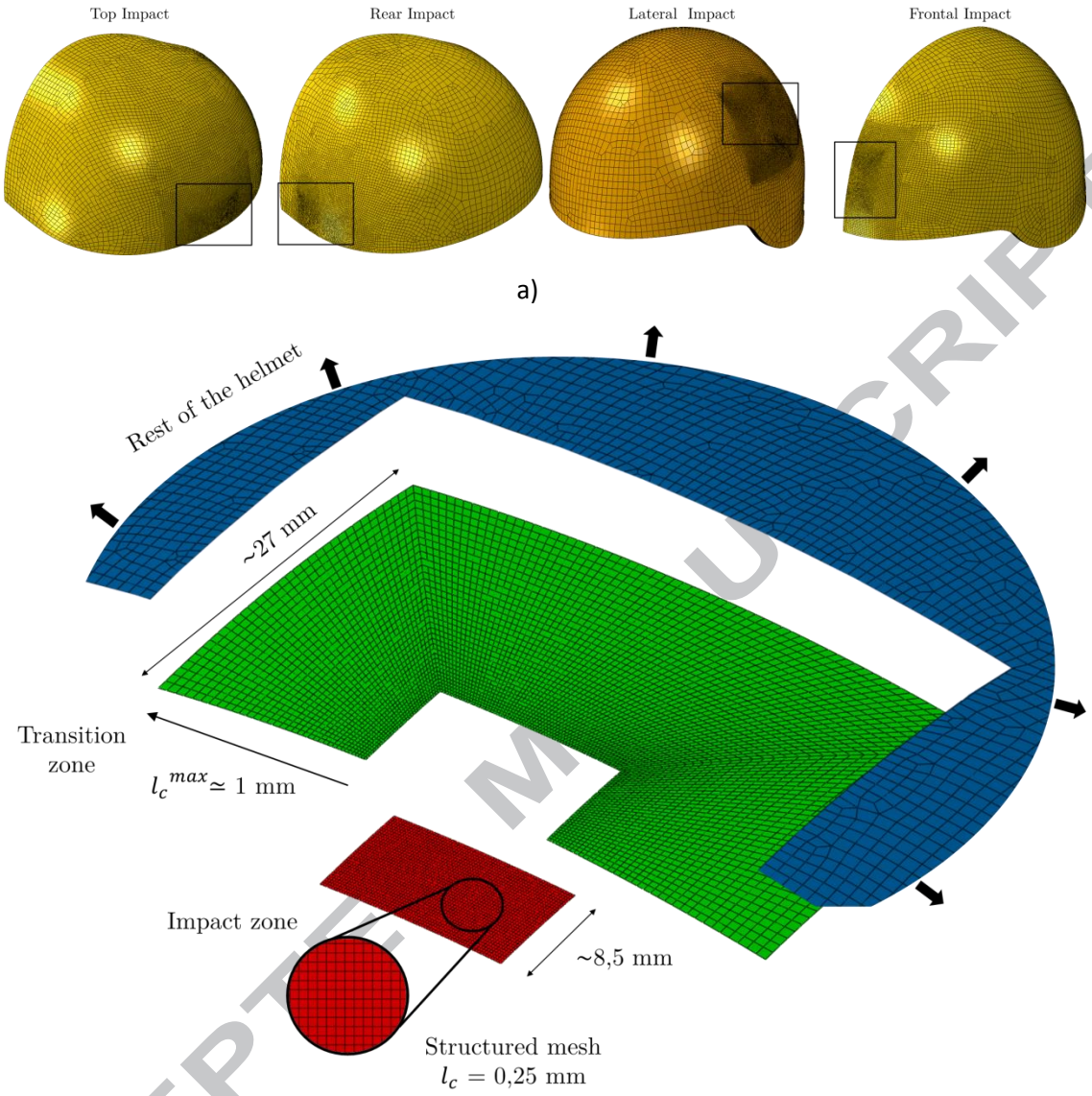

Figure 11. Helmet mesh model. a) Different impact locations. b) Refined-mesh detail and transition zone.

The numbers of elements per layer varies depending on the impact location case (table 7),

Impact location	Elements
Frontal	12889
Top	13815
Rear	12386
Lateral	25690

Table 7. Number of elements per layer for different impact locations

The boundary conditions consist of the complete movement restriction of the nodes corresponding to the gripped surface by jaws in the experimental tests.

Next figure shows some detailed frames corresponding to numerical impact tests simulated at the frontal, lateral, rear and top zone against FSP.

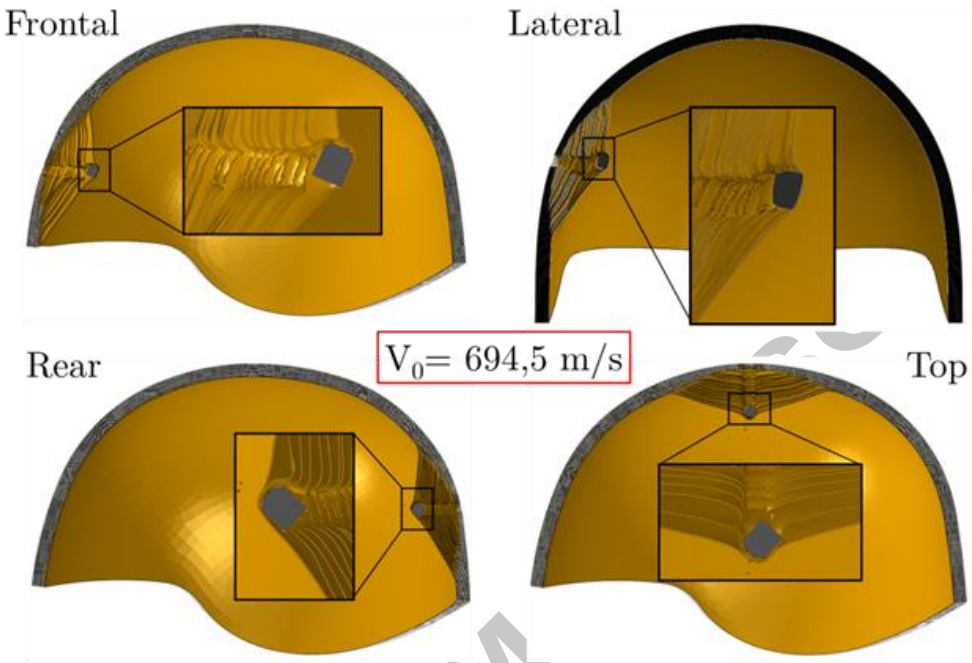

Figure 12. Numerical simulation of FSP impacts at 697 m/s on Combat Helmet for different impact locations

The numerical results cover an impact velocity range from 692 m/s to 810 m/s for FSP (Figure 13a) and 600 m/s to 750 m/s for spheres. (Figure 13b). The maximum impact velocity without complete perforation was evaluated numerically for each location, obtaining 697 m/s for Frontal and Vertical location, 698m/s for Rear impact and 686 m/s for Lateral location. The average of these values is in good agreement with the experimental V_{50}, obtaining 694,5 m/s in numerical simulations and 697 m/s for the experimental test (Figure 13).

The ballistic limits obtained in numerical simulations for each impact location are 622 m/s for Frontal, 616 m/s for vertical, 620 m/s in rear impact and finally 616 m/s for lateral location. These ballistic limit values are close to experimental ballistic limit, which is 608 m/s approximately.

Figure 13a and Figure 13b present experimental and numerical residual velocity compared to impact velocity for the considered cases, showing a general good agreement. Differences in some cases are attributed to small impact dealignment during helmet gripping.

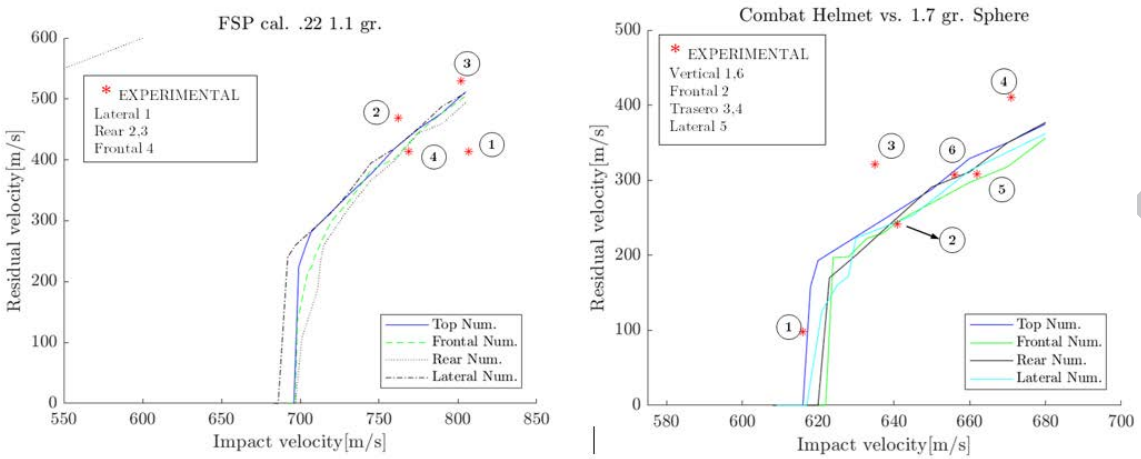

a) b)

Figure 13. Comparison of residual velocity V_r versus impact velocity V_0 between experiments and numerical simulations for: a) FSP b) spherical steel projectile.

Although the ballistic limit of has been validated for an 8.86 kg/m^2 areal density helmet, its variation with different areal densities for both projectiles is analyzed in Figure 14. In case of 7.75 kg/m^2, that corresponds to a 12,5% lighter helmet than the reference one, the ballistic limit decreases less than 6% for both projectiles. Additionally, 11.44 kg/m^2 areal density used in other different combat helmet studies [4, 11] is considered. Here, for a 22% heavier case, the ballistic limit prediction increases less than 9% for both projectiles.

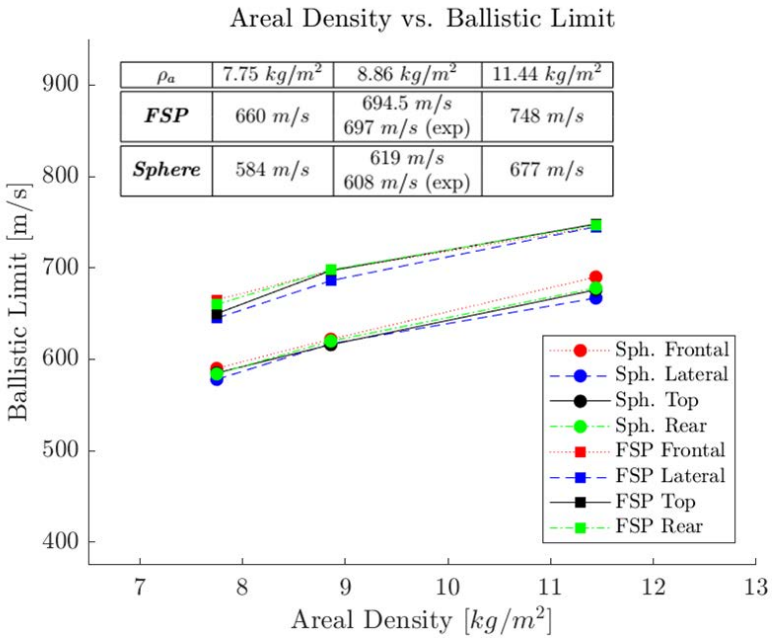

Figure 14. Numerical analysis of areal densities of combat helmet.

4.4. Damage Analysis

An analysis of the internal helmet damage after impacts is carried out through observations of the post-experimental CT scans and compared with the corresponding numerical prediction. The

CT equipment used, a *Phoenix v/tomex* of *GE Sensing and Inspection Technologies X Ray* company, has an x-ray tube with a 140 kV nanofocus. A detail of the frontal impact case is presented in Figure 15. The failure mechanisms in the helmet can be seen: shear plugging and compression, delamination and tensile breakage of the last fibres. The predictions of the numerical model are considerably similar to the post-impact CT scan observations. Other authors have used the computed tomography (CT) technique to analyze the damage induced in combat helmets against impact event [5].

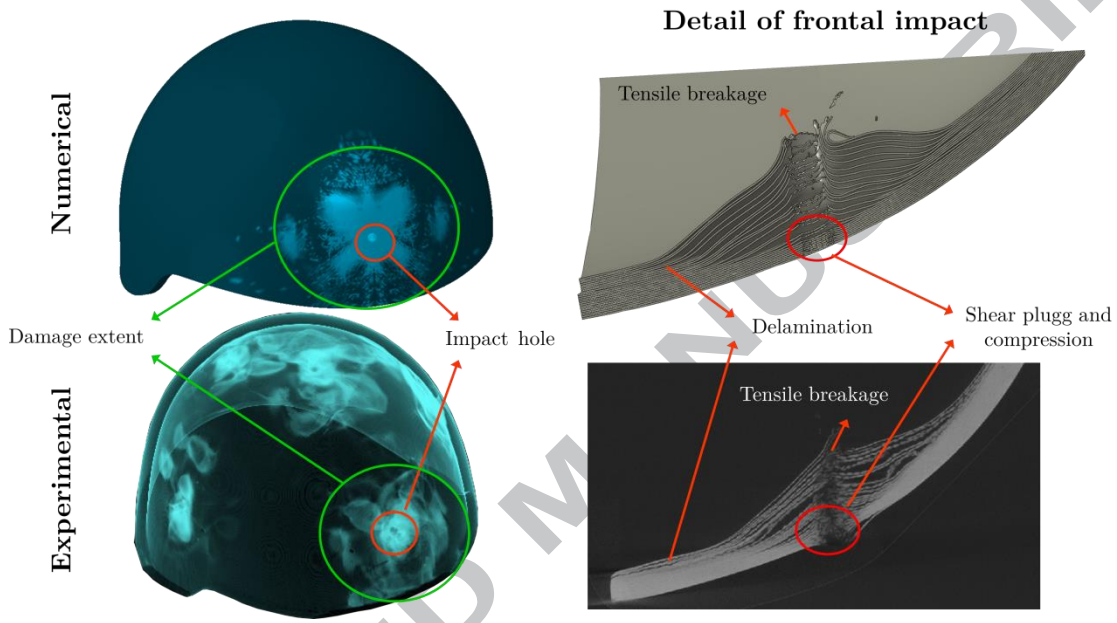

Figure 15. Comparison of post-experimental CT scans (bottom) and numerical simulations (top)

As the figure shows, damage after impacts varies through the thickness of the combat helmet. As mentioned before, the first damage stage is shear plugging and compression, is localised and is nearly the diameter of the projectile. The mode of failure that produces the most significant extent of damage is the delamination. This damage mode is predominant at energy absorption [1]. The quantification of damage extent produced is relevant to know how much of the helmet is damaged.

The analysis is carried out for the different locations where the impacts were performed for FSP and steel spheres. The damage measure method is presented in Figure 16 where damage extent is approximated by an ellipse area which axes are both perpendicular directions of damage extent.

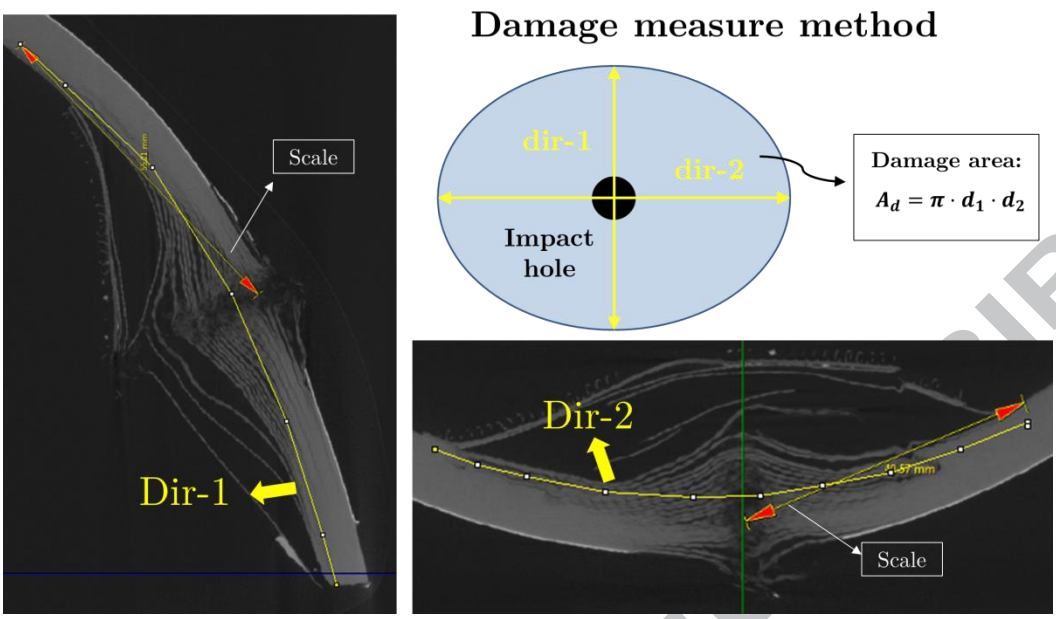

Figure 16. Damage measure method.

Damage extent area due to FSP and sphere projectile are presented for different impact locations in Figure 17. In general, numerical results provided a good correlation between experimental results and damage calculated in simulations. The maximum damage is produced at the Top helmet zone, where delamination propagates easily. For FSP projectiles (Fig. 17a), the maximum error is 7% and it is produced at Frontal impact. On the other side, for steel spheres projectiles impacted at lower velocities than in FSP cases, the damage extension is quite similar for the different impact positions. Numerical simulations are in good agreement with experimental damage results with less than 3% error.

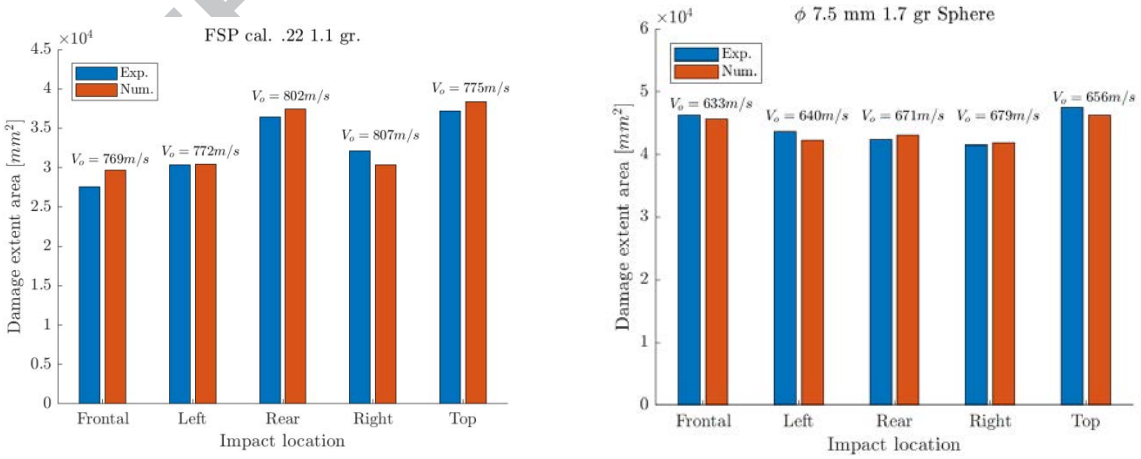

a) . b)

Figure 17. Damage analysis according to impact location, a) FSP projectile, b) Sphere projectile

Close to the ballistic limit, as mentioned in the case of flat plate tests, there is a high projectile kinetic energy transference to the helmet delamination. However, when impact velocity

increases far beyond the ballistic limit, damage effects are more localized. This effect is also observed in other materials against ballistic impact [31,32].

From numerical simulations and CT inspections, see Figure 15, it can also be determined the length of the perforation cavity. Figure 17 presents the compared results for this damage parameter. The maximum error between tests and predictions are the range of 3-22% for FSP and 0-22% for spheres, considered in an adequate agreement. Below the ballistic limit, this damage parameter helps to determine the minimum required distance between the internal helmet surface and the head (helmet size), relate to the Back-Face Deformation.

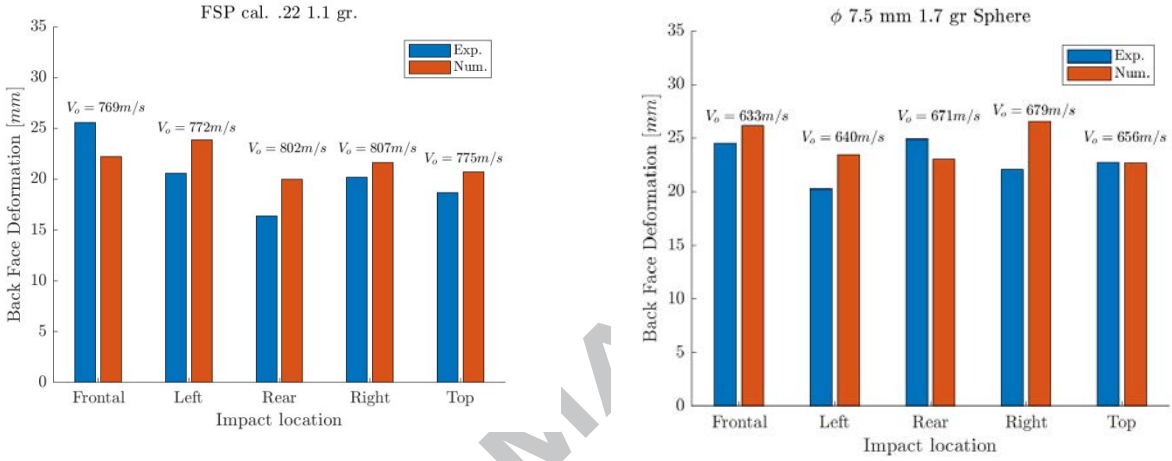

a) b)

Figure 17. Back Face Deformation analysis according to impact location, a) FSP projectile, b) Steel sphere projectile

5. Conclusions

In this work, a numerical model for combat helmets of aramid composites against two kinds of ballistic projectiles (1.1g FSP and 1.7g steel sphere) has been developed for designing purposes.

First of all, the proposed numerical model has been calibrated with experimental impact tests on aramid flat-plates of two different thicknesses, being analyzed the ballistic curve, failure mechanics and back-face displacement. The numerical model for aramid composite presented has the same number of layers as the specimens, considering one element per layer through the thickness and cohesive surface between them. This novel configuration allows to capture the ballistic aramid behavior but also the damage induced in the aramid composite included delamination effects at the interface between layers.

Once the model is calibrated, numerical results are compared to experimental tests carried out for both projectiles commonly impacting on real combat helmets. Attending to the obtained results, the impact zone has a significant influence on the ballistic limit and in the induced damage. This is attributed to the influence of the boundary conditions, as the proximity to the free-boundaries or to the helmet clamping zone. In general, impact close to the free boundary, where it is easier to deform, required higher impact velocity for complete perforation. In the case of FSP, where predominant damage mechanism is shear failure, lateral impact is the most critical situation due to the proximity of clamping devices enhancing the stiffness of the

component in this zone, increasing the shear effects. For impact velocities far above the ballistic limit, the impact zone location has no significant importance.

Apparently, ballistic impact induces a very localized damage area close to the impact zone. The consideration of cohesive interlayers allows to determine the delamination area extension, that increased with the impact velocity up to the ballistic limit. This extended area values are several times larger than the projectile section and can compromise the residual integrity of the helmet. This area diminishes with the velocity far above the ballistic limit, converging to the projectile section. The inclusion of cohesive elements allows to determine the transversal damage during perforation that leads to the back-face deformation. By means of this model, a better estimation of the minimum required distance from the back-face helmet to the head can be achieved.

The areal density effect in the ballistic analysis of combat helmet is also analyzed close to the reference value. Its relationship with the ballistic limit can be considered linear in the analyzed range. This can be of great help when designing combat helmets that meet the requirements of STANAG 2920.

Therefore, the numerical combat helmet model developed in this work captured the mechanical behaviour of aramid composites under small projectile impacts regarding the residual velocity, ballistic limit and deformations. An important novelty is the modelling of each layer and the interlaminar failure, that allows to estimate the damage extension and the back-face deformation. In the authors' opinion, this should be analyzed together with the ballistic behaviour in future works on helmets made of aramid or other materials.

Acknowledgements

The authors acknowledge the Ministry of Economy and Competitiveness of Spain and FEDER program under the Project RTC-2015-3887-8 and the Project DPI2017-88166-R for the financial support of the work. Also, authors are indebted to the Spanish company FECSA for providing the helmets tested in the paper and to CENIEH for carrying out the CT scans.

6. References

[1] Kulkarni, S. G., Gao, X. L., Horner, S. E., Zheng, J. Q., & David, N. V.. Ballistic helmets–their design, materials, and performance against traumatic brain injury. Composite Structures, 2013; 101, 313-331.

[2] Justice NI of. NIJ Standard for Ballistic Helmets. 1981.

[3] NATO Standarization Agency. STANAG 2920 PPS (Edition 2) - Ballistic test method for personal armour materials and combat clothing. 2003.

[4] Tham CY, Tan VBC, Lee HP. Ballistic impact of a KEVLAR® helmet: Experiment and simulations. Int J Impact Eng 2008;35:304–18. doi:10.1016/j.ijimpeng.2007.03.008.

[5] Tan L Bin, Tse KM, Lee HP, Tan VBC, Lim SP. Performance of an advanced combat helmet with different interior cushioning systems in ballistic impact: Experiments and finite element simulations. Int J Impact Eng 2012;50:99–112.

doi:10.1016/j.ijimpeng.2012.06.003.

[6] Rodriguez-Millan M, Ito T, Loya JA, Olmedo A, Miguelez MH. Development of numerical model for ballistic resistance evaluation of combat helmet and experimental validation. Mater Des 2016;110:391–403. doi:10.1016/j.matdes.2016.08.015.

[7] Barrett J. Design validation of future ballistic neck protection through the development of novel injury models. University of Birmingham, 2015.

[8] Nayak N, Banerjee A, Datta D. Ultrasonic assessment of bullet inflicted damage in aramid laminated composites. Def Sci J 2012;62:153–8. doi:10.14429/dsj.62.1467.

[9] Nayak N, Banerjee A, Panda TR. Numerical Study on the Ballistic Impact Response of Aramid Fabric- epoxy Laminated Composites by Armor Piercing Projectile. Procedia Eng 2017;173:230–7. doi:10.1016/j.proeng.2016.12.002.

[10] Colakoglu M, Soykasap O, Army T, Özek T. Experimental and Numerical Investigations on the Ballistic Performance of Polymer Matrix Composites Used in Armor Design. Appl Compos Mater 2007;2:1–8. doi:10.1007/s10443-006-9030-y.

[11] Van Hoof J, Cronin DS, Worswick MJ, Williams K V, Nandlall D. Numerical Head and Composite Helmet models to predict blunt. 19th Int. Symp. Ballist. 7–11 May 2001, Interlaken, Switz., 2001, p. 7–11.

[12] Lee HP, Gong SW. Finite element analysis for the evaluation of protective functions of helmets against ballistic impact. Comput Methods Biomech Biomed Engin 2010;13:537–50.

[13] Li YQ, Li XG, Gao X-L. Modeling of Advanced Combat Helmet Under Ballistic Impact. J Appl Mech 2015;82:111004-1–9. doi:10.1115/1.4031095.

[14] Palta E, Fang H, Weggel DC. Finite element analysis of the Advanced Combat Helmet under various ballistic impacts. Int J Impact Eng 2018;112:125–43. doi:10.1016/j.ijimpeng.2017.10.010.

[15] Jenson, D., & Unnikrishnan, V. U. Energy dissipation of nanocomposite based helmets for blast-induced traumatic brain injury mitigation. Composite structures, (2015) 121, 211-216.

[16] Palomar, M., Lozano-Mínguez, E., Rodríguez-Millán, M., Miguélez, M. H., & Giner, E. Relevant factors in the design of composite ballistic helmets. Composite Structures, (2018) 201, 49-61.

[17] Aare, M., & Kleiven, S.. Evaluation of head response to ballistic helmet impacts using the finite element method. International Journal of Impact Engineering, (2007), 34(3), 596-608.

[18] Tse, K., Tan, L., Yang, B., Tan, V., Lim, S., & Lee, H.. Ballistic impacts of a Full-Metal Jacketed (FMJ) bullet on a validated Finite Element (FE) model of helmet-cushion-head. 5th International Conference on Computational Methods (ICCM2014), Cambridge, UK, July (pp. 28-30).

[19] Tse, K. M., Tan, L. B., Yang, B., Tan, V. B. C., & Lee, H. P.. Effect of helmet liner systems and impact directions on severity of head injuries sustained in ballistic impacts: a finite element (FE) study. Medical & biological engineering & computing, (2017), 55(4), 641-

662.

[20] Tan LB, Chew FS, Tse KM, Chye Tan VB, Lee HP. Impact of complex blast waves on the human head: a computational study. Int J Numer Method Biomed Eng 2014:1–30. doi:10.1002/cnm.2668.

[21] Rodríguez-Millán M, Tan LB, Tse KM, Lee HP, Miguélez MH. Effect of full helmet systems on human head responses under blast loading. Mater Des 2016;117:58–71. doi:10.1016/j.matdes.2016.12.081.

[22] Li XG, Gao XL, Kleiven S. Behind helmet blunt trauma induced by ballistic impact: a computational model. Int J Impact Eng 2016;91:56–67. doi:10.1016/j.ijimpeng.2015.12.010.

[23] Gower H. L., Cronin D.S., Plumtree A. Ballistic impact response of laminated composite panels, International journal of impact engineering, pp. 1000-1008, 2008.

[24] Hou, J. P., Petrinic, N., Ruiz, C., & Hallett, S. R.. Prediction of impact damage in composite plates. Composites Science and Technology, 2000 60(2), 273-281.

[25] F. Chang, K. A. Chang. A progressive damage model for laminated composites containing stress concentrations. Journal of composite materials 1987, pp. 834-855.

[26] Rodríguez Millán M, Moreno CE, Marco M, Santiuste C, Miguélez H. Numerical analysis of the ballistic behaviour of Kevlar® composite under impact of double-nosed stepped cylindrical projectiles. J Reinf Plast Compos 2015;35:124–37. doi:10.1177/0731684415608004.

[27] Van Hoof J, Deutekom MJ, Worswick MJ, Bolduc M. Experimental and numerical analysis of the ballistic response of composite helmet materials. In: 18th International symposium on ballistics. San Antonio, TX, USA; 1999.

[28] Van Hoof J, Cronin DS, Worswick MJ, Williams KV, Nandlall D. Numerical head and composite helmet models to predict blunt trauma. In: 19th International symposium on ballistics. Interlaken, Switzerland; 2001.

[29] Materials Data Book. 2003 Edition. Cambridge University Engineering

[30] Moure, MM., Rubio, I., Aranda-Ruiz, J., Loya, J.A., & Rodríguez-Millán, M. Analysis of impact energy absorption by lightweight aramid structures. Composite Structures, (2018). 203, 917-926.

[31] Davies, G. A. O., & Robinson, P. Predicting failure by debonding/delamination. AGARD, Debonding/Delamination of Composites 1992 28 p(SEE N 93-21507 07-24).

[32] Systèmes D. Abaqus v6.14 Documentation- ABAQUS Analysis User's Manual ABAQUS. 2014th ed. 2014.

[33] Rodríguez-Millán M, Vaz-Romero A., Rusinek A., Rodríguez-Martínez J.A., Arias A. Experimental Study on the Perforation Process of 5754-H111 and 6082-T6 Aluminium Plates Subjected to Normal Impact by Conical, Hemispherical and Blunt Projectiles. Exp Mech 2014;54:729–42. doi:10.1007/s11340-013-9829-z.

[34] Rodriguez-Millan M, Garcia-Gonzalez D, Rusinek A, Abed F, Arias A. Perforation mechanics of 2024 aluminium protective plates subjected to impact by different nose

shapes of projectiles. Thin-Walled Struct 2018;123:1–10. doi:10.1016/j.tws.2017.11.004.